ADVANCED FUNCTIONAL MATERIALS
www.afm-journal.de

Check for updates

Bottom-Up Growth of Graphene Nanospears and Nanoribbons

Haibin Sun, Fengning Liu, Leining Zhang, Kyungmin Ko, Ben McLean, Hao An, Sungkyun Kim, Ming Huang, Marc-Georg Willinger, Rodney S. Ruoff, Joonki Suh, Zhu-Jun Wang,* and Feng Ding**

One dimensional graphene nanostructures are one of the most promising materials for next generation electronics. Here, the chemical vapor depostion growth of graphene nanoribbons (GNRs) and graphene nanospears (GNSs) on a copper surface is reported. The growth of GNRs and GNSs is enabled by a vapor–liquid–solid (VLS) mechanism guided by on-surface propagation of a liquid Cu-Si catalyst particle. The slow lateral growth and the fast VLS vertical growth give rise to spear head-shaped GNSs. In situ observations further confirm that the lateral graphene growth can be completely suppressed and thus GNRs are grown. The synthesized field effect transistor (FET) devices show that the GNRs and GNSs have high carrier mobilities of ≈2000 $cm^2 V^{-1} s^{-1}$. Both FET and Kelvin probe force microscopy measurements confirm that the Fermi levels of the synthesize GNSs shift downward from the wide part to the tip is strongly *p*-doped. These findings yield key insights into the growth mechanism of graphene and open a door for achieving a facile and scalable method of synthesizing free standing GNRs and GNSs and their applications, such as the Fermi-level tunable devices.

1. Introduction

Graphene nanoribbons (GNRs), inherit properties from large 2D graphene such as high mobility,[1] high mechanical,[2] and thermal stability.[3] Notably, GNRs exhibit a bandgap that can be tuned depending on the GNR width and its crystallographic orientation,[4] and therefore offer exciting opportunities for application in electronics.[5] However, applications of GNRs is greatly hindered by the challenge of their difficult synthesis.

Top-down methods of GNRs synthesis, such as unzipping carbon nanotubes[6] and etching graphene,[7] have proven challenging, as they commonly introduce defects and irregular edge structures at low yields with difficulty in controlling GNR width. For the last decade,[8] bottom-up synthesis of GNRs from aromatic molecular frameworks has seen more success, despite often requiring costly ultra-high vacuum (UHV) conditions,[9] and those based in solution are difficult to transfer to insulating substrates and edge functionalization can diminish favorable optoelectronic properties.[10] Chemical vapor deposition (CVD) presents a facile alternative to bottom-up GNR synthesis and has been utilized to grow GNRs on Au(111) surfaces[11] though often have imperfect edges and short lengths. Cu(111) provides a more accessible substrate for GNR synthesis though has only been successful under UHV conditions.[12] Recently, controlled growth of oriented GNRs via CVD was achieved in etched hBN channels on a quartz substrate,[13] and suspended GNR arrays were synthesized in high yield on Ni following plasma CVD and

H. Sun, F. Liu, L. Zhang, B. McLean, H. An, S. Kim, M. Huang, R. S. Ruoff, F. Ding
Center for Multidimensional Carbon Materials
Institute for Basic Science (IBS)
Ulsan 44919, Republic of Korea

H. Sun
Key Laboratory of Microelectronics and Energy of Henan Province
College of Physics and Electronic Engineering
Xinyang Normal University
Xinyang 464000, China

F. Liu, K. Ko, H. An, R. S. Ruoff, J. Suh, F. Ding
Department of Materials Science and Engineering
Ulsan National Institute of Science and Technology
Ulsan 44919, Republic of Korea
E-mail: jsuh@unist.ac.kr; f.ding@unist.ac.kr

The ORCID identification number(s) for the author(s) of this article can be found under https://doi.org/10.1002/adfm.202206961.

M.-G. Willinger, Z.-J. Wang
Scientific Center for Optical and Electron Microscopy
ETH Zurich
Otto-Stern-Weg 3, Zurich 8093, Switzerland

R. S. Ruoff
Department of Chemistry
Ulsan National Institute of Science and Technology (UNIST)
Ulsan 44919, Republic of Korea

R. S. Ruoff
School of Energy and Chemical Engineering
Ulsan National Institute of Science and Technology (UNIST)
Ulsan 44919, Republic of Korea

Z.-J. Wang
School of Physical Science and Technology
Shanghai Tech University
Shanghai 200031, China
E-mail: wangzhj3@shanghaitech.edu.cn

DOI: 10.1002/adfm.202206961

 © 2022 Wiley-VCH GmbH

cooling,[14] however the mechanisms of growth for each case lack understanding.

Here, a unique approach to CVD growth of GNRs on a Cu surface is reported. Atmospheric pressure CVD graphene growth yields graphene islands exhibiting a variety of shapes including the formation of what we term graphene nanospears (GNSs). The mechanism of GNSs growth is different from CVD graphene[15] that is typically grown via a vapor–solid–solid (VSS) mechanism, where individual graphene islands nucleate and grow from precursor decomposition and addition to the graphene edge on the Cu surface.[16] The observed sharp GNS structures form as a result of a suppression of the VSS growth of graphene in favor of vapor–liquid–solid (VLS)[17] growth of a central GNR structure. By controlling H_2 flow in a flexible in situ scanning electron microscopy (SEM) system, the complete suppression of VSS growth leads to the VLS-grown GNRs. In other words, 2D VSS graphene growth is degenerated in favor of 1D VLS GNR growth. Besides, it is demonstrated that the surface potential of GNS is dependent on the width and thus Fermi energy tunable electronic devices might be built with by using GNSs as the base material. The experimental findings, obtained here for the case of graphene, are confirmed by theory-based growth simulations, and can be generalized to other 2D materials. Based on the gained understanding of the 2D VLS evolution, conditions for the optimization of scalable production of 2D materials are established.

2. Results

2.1. Growth and Characterization of the Graphene Islands

Performing atmospheric pressure CVD at 1050 °C, with 150 sccm of diluted CH_4 and 200 sccm of H_2 (Figure S1a, Supporting Information), we observe graphene islands presented in **Figure 1**a–h and Figures S2 and S3 (Supporting Information). Consistent with previous graphene growth on Cu foils, a large number of graphene islands are hexagonal shaped (Figure 1b). Interestingly, graphene islands exhibiting a range of other shapes are also observed. Figure 1c–h shows SEM images of graphene islands with elongated, sharp tips that terminate in a particle. Graphene islands with one or more

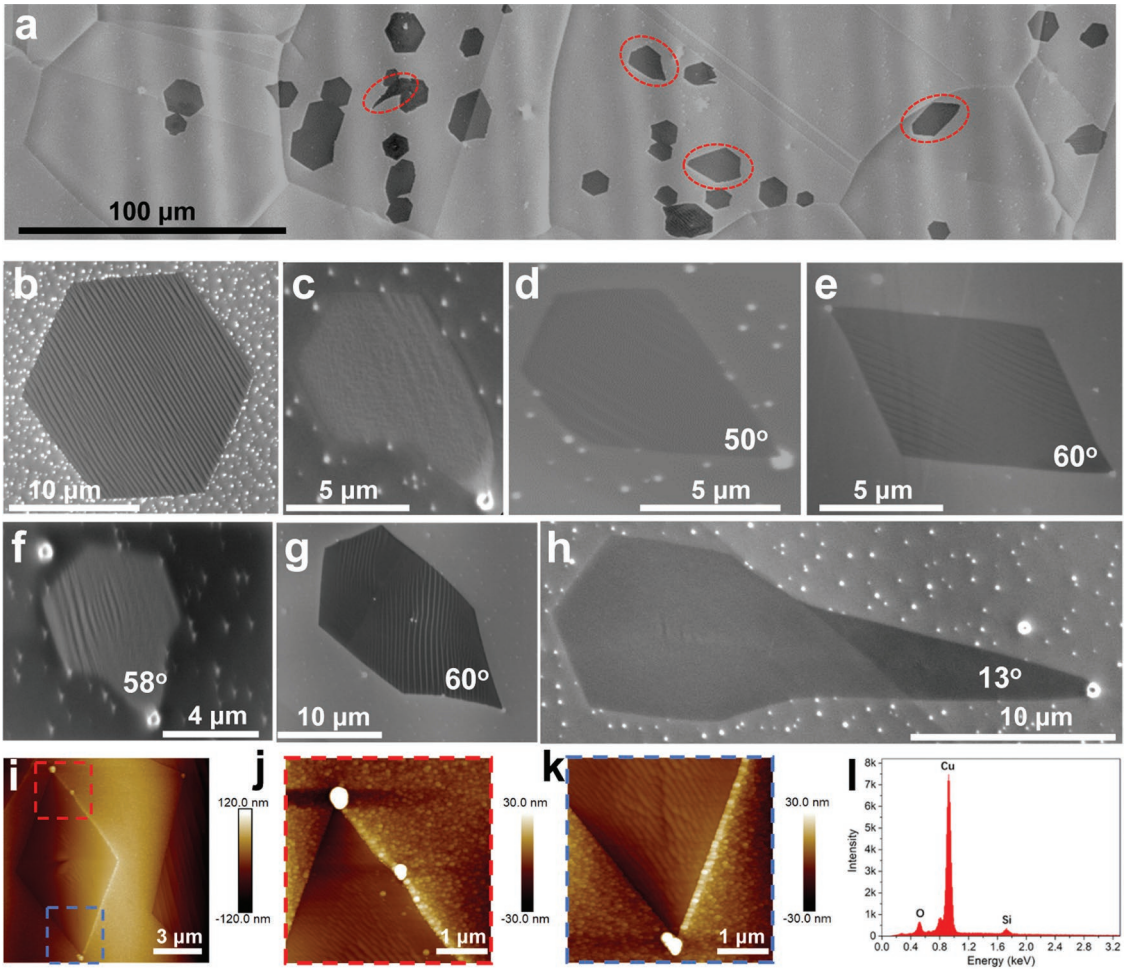

Figure 1. Catalyst particle-mediated graphene islands grown on Cu foil. a) SEM image of graphene islands with different shapes; b) hexagonal graphene island typically observed following CVD growth; c–h) catalyst-mediated graphene growth resulting in various graphene island shapes with particles (white) attached to the tips and many particles present on Cu foil; i–k) AFM images of a parallelogram-shaped graphene island grown on Cu and the magnified zones with catalyst particles; l) EDS spectrum of the catalyst particle, showing strong Si and O signals.

© 2022 Wiley-VCH GmbH

particles attached to the tips take the shape of various irregular polygons. As shown in Figure 1e, a parallelogram-shaped island is present when there are two particles attached, with the two sharp tips having tip angles of ≈60°. Tip angles ranging from 13° to 60° are observed. Sharp tip angles are only observed in the presence of a particle at the tip, making it clear that these particles play a crucial role during the growth process of these graphene islands with sharp tips. Figure 1i–k presents the atomic force microscopy (AFM) image of a parallelogram-shaped graphene island and the magnified images of its two sharp tips, with particles clearly attached. Since the quartz tube is mainly composed of SiO_2, it is unavoidable to introducing Si content to the Cu substrate under a H_2 environment during the heat treatment.[18] Figure 1l is the energy-dispersive x-ray spectroscopy (EDS) analysis of the particle surface, showing significant Si and O contents in it. X-ray photoelectron spectroscopy (XPS) shown in Figure S4 (Supporting Information) spectra also displays strong Si-2p, O-1s signals, which further confirms the silicon and oxygen contents on the Cu surface. Based on the observed coalescence behavior of these particles (presented in Figure 4), we can deduce that these particles are in a liquid state with a melting point lower than the experimental temperature (1050 °C). Therefore, these particles are notably not SiO_2 particles (melting point 1710 °C) as observed in most CVD experiments for graphene growth. In addition, from the phase diagram of Cu–Si,[19] we find that a $Cu_{(1-x)}Si_x$ alloy with x from 0.15 to 0.3 has the melting point of ≈850 °C. It is reasonable to guess that the particle is then a Cu-rich liquid Cu–Si alloy although the exact content cannot be determined in this system.

On a Cu surface, the propagation of graphene edge is the consequence of adding carbon atoms from vapor phase, hence the VSS growth mechanism. The typical hexagonal shape of graphene islands is due to anisotropic growth of the graphene lattice with a six-fold symmetry. As a result of the slow VSS propagation of the zigzag (ZZ) edge, each side of the hexagonal island comprises of ZZ edges.[20] According to the crystal growth kinetics, the formation of a sharp-tipped graphene island requires a faster growth rate along the direction of the bisect angle of the tip.[16b,20d,21] Here each sharp tip corresponds to the presence of a particle hence the particles are responsible for the faster growth rate and the symmetry breaking of graphene growth.

2.2. Mechanism of the Graphene Nanospears and Nanoribbons Growth

To understand how a particle facilitates the graphene growth, we recall the VLS growth mechanism of nanowires and carbon nanotubes.[22] In this model, feedstock from the vapor phase adsorbs to the liquid phase catalyst particle that facilitates decomposition of the precursors and subsequent attachment to the solid nanowire or nanotube. Recently, the VLS growth of 2D materials has been observed in the growth of ultralong MoS_2 nanoribbons.[23] Here, we use the combination of the liquid catalyst-guided VLS GNR growth and the general VSS graphene growth to explain the formation of the various shapes of graphene islands observed in Figure 1. As shown in **Figure 2**a, the propagation of a liquid particle on Cu surface leads to the formation of a GNR behind it (the black ribbon) while simultaneously, slower VSS growth of the GNR edge leads to a surrounding graphene layer (the gray area). The angle, β of the spear-like tip is

$$\beta = 2\sin^{-1}\left(\frac{R_{VSS}}{R_{VLS}}\right) \quad (1)$$

where R_{VSS} and R_{VLS} are the VSS and VLS growth rates of graphene, respectively. From Equation (1), we can clearly see that the shape of the graphene nanospear can be tuned by varying R_{VSS}, R_{VLS} or both. As shown in Figure 2a,b, sharp graphene nanospear can be formed if $R_{VLS} \gg R_{VSS}$. Critically, if the VSS graphene growth is completely suppressed, a GNR will be formed by catalyst guided VLS growth (Figure 2c).

Following the proposed mechanism, we illustrate the growth process of a few graphene islands guided by the propagation of the catalyst particles. Figure 2d1–d4 corresponds to the growth mechanism of the graphene island in Figures 1f–h. Figure 2e1–e4 present the growth process of the graphene island in Figure 1c,d. Figure 2f1–f4 predicts how the parallelogram in Figure 1e may form. The observed graphene islands have all formed as a result of the proposed VSS + VLS mechanism, with the liquid catalyst particle propagating across the Cu surface.

2.3. Synthesis of the Graphene Nanospears

We demonstrate that the shape of the graphene nanospear can be tuned by varying the experimental condition. By increasing the H_2/CH_4 ratio, which has previously been shown to facilitate the etching of graphene and slow down the VSS growth rate,[7d,24] we have successfully synthesized very sharp GNSs, comprising of a central GNR (**Figure 3**a,b; Figure S5, Supporting Information). The SEM images of a typical GNS with a tip angle of 10° is shown in Figure 3c,d. This tip angle implies that the VLS growth rate is ≈10 times that of the VSS growth rate. In the central part of Figure 3d, a narrow ribbon-like track can be clearly seen. After it was transferred to a SiO_2 surface, a dark line of ≈200 nm wide is notable (Figure 3e), indicative of a GNR, supporting the proposed two-step mechanism shown in Figure 2. The central GNR is grown via the VLS mode guided by the liquid catalyst particle while the surrounding graphene is grown via the VSS mode. The AFM image (Figure 3f) confirms that the central GNR is different from the surrounding graphene. Figure 3g measures the size of the catalyst particle to be 100 nm in height and the GNR to be 50 nm in width. Furthermore, statistical result shown in Figure 3h presents that the tip angles of these GNSs are distributed in a small range between 1° to 12°, implying that increase H_2/CH_4 ratio can greatly increase the ratio of R_{VLS} to R_{VSS} by suppressing the VSS graphene growth. The growth mechanism of the central VLS GNR is illustrated in Figure 3i, where the precursor molecules (CH_4) decompose on the Cu substrate and the released C atoms diffuse to the liquid catalyst particle. The liquid catalyst particle facilitates the attachment of C atoms to an end of central GNR by overcoming a lower reaction barrier than that of VSS graphene growth.

© 2022 Wiley-VCH GmbH

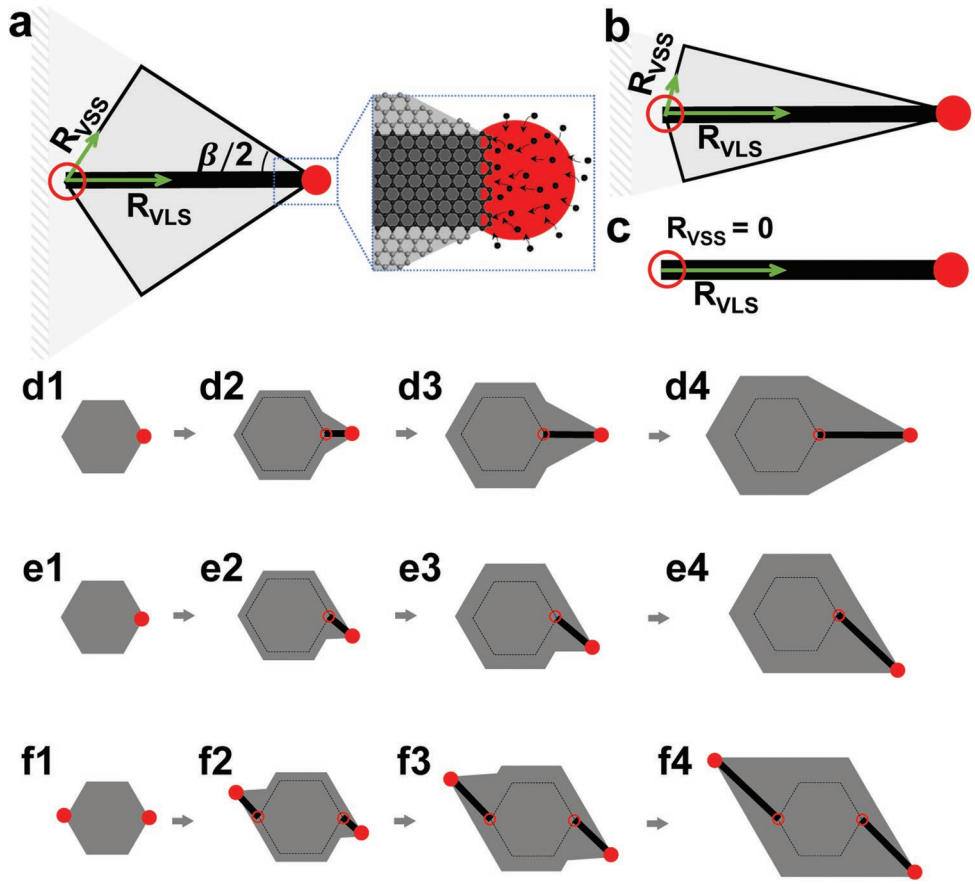

Figure 2. The mechanism of catalyst particle mediated graphene growth. a) A liquid catalyst particle (red circle) moves forward at the rate of R_{VLS} initiating continuous vapor–liquid–solid (VLS) growth of GNR (black line) behind it. The normal VSS growth of graphene (gray area) on Cu surface leads to a GNS with tip angle of β, where R_{VSS} is the graphene growth rate on Cu foil ($R_{VLS} > R_{VSS}$). b) Slower VSS graphene growth compared to the VLS GNR growth leads to a sharper GNS ($R_{VLS} >> R_{VSS}$). c) Suppressing the VSS graphene growth completely ($R_{VSS} = 0$) leads to only GNR growth. d1→d2→d3→d4) A liquid catalyst particle attached to a hexagonal graphene island initiates VLS GNR growth toward the right and leads to an elongated hexagon with a sharp tip. e1→e2→e3→e4) A liquid catalyst particle attached to a hexagonal graphene island initiates diagonal GNR growth and leads to an elongated pentagon with a sharp tip. f1→f2→f3→f4) Two liquid catalysts particles attached to a hexagonal graphene island initiate the growth of two GNRs diagonally leads to a parallelogram-shaped graphene island with two sharp tips.

2.4. Real-Time Real-Space Characterization of GNR Growth

The observations in Figure 3 support our hypothesis that the growth of a GNS contains a VLS-grown GNR central to the VSS-grown graphene edges. However, our thermal CVD system is incapable of reliably tuning the experimental condition to fully suppress VSS growth of graphene surrounding the GNR. To realize the VLS growth of the GNR while suppressing the VSS growth, we employ a more flexible operanto SEM system. **Figure 4** (a1→a2→a3→a4) demonstrates the real-time and real-space growth of a GNR via operanto SEM. The GNR grows in length by ≈120 nm s^{-1} with no significant change in width. During the whole growth process, the width of the GNR remains ≈500 nm, implying that in-plane VSS growth is completely suppressed. In turn, this suggests that the activation energy of graphene VSS growth is much higher than that of maintaining graphene VLS growth facilitated by the catalyst particle.

Figure 4(b1→b2→b3→b4→b5) presents another example of GNR growth by operanto SEM, during that the catalyst particle becomes smaller and smaller and finally disappears from view. As the catalyst particle appears to shrink, the growth of the GNR slows and the width gradually decreases until growth ceases at 104.5 s after the catalyst disappears. This observation highlights the critical role of the catalyst particle in growth, in support of the VLS growth mechanism.

Figure 4(c1→c2→c3→c4) demonstrates the liquid nature of the catalyst particles on the Cu surface under the growth condition. During this evolution, it can be clearly seen that particles 1, 2, and 3 merge into a large particle after 72 s; while particle 4, increasing gradually in size, diffuses toward the newly formed particle over 108 s. The quick coalescence and diffusion of ≈100 nm diameter catalyst particles strongly support the liquid state of these particles, as discussed above.

To investigate the charge transport characteristics of GNS structure, the field-effect transistors were fabricated and measured with a back-gate configuration (**Figure 5**a). Their room-temperature mobility was estimated to be 1801

© 2022 Wiley-VCH GmbH

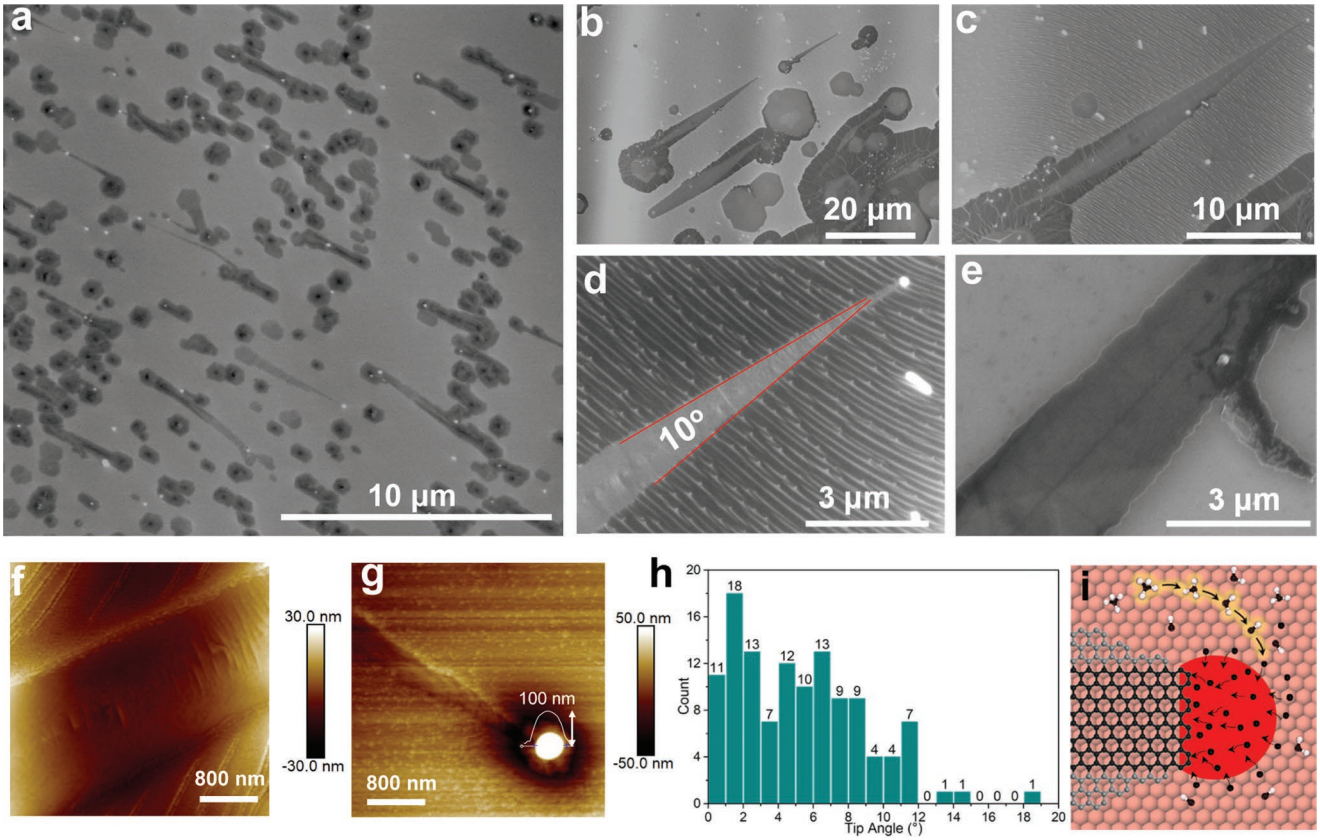

Figure 3. The growth of sharp GNSs comprising GNRs on Cu foil. a) SEM image showing approximately 20% of graphene islands grow as GNSs after increasing the H_2 flow rate from 200 to 300 sccm. b–d) GNSs with different magnifications by SEM. d) Magnified SEM image showing the tip angle of this GNS is only 10°. e) Magnified SEM image of a GNS transferred to SiO_2 surface clearly showed a central GNR within the GNS. f,g) AFM images of the GNS wall and tip, within that the central GNR can be seen. Particle measured to be ≈100 nm in diameter. h) Statistical results showing the distributions of tip angles. i) A schematic model showing the growth mechanism of the central VLS GNR and GNS.

and 420 $cm^2\ V^{-1}\ s^{-1}$ for the "narrow" and "wide" channels of GNS, respectively (Inset of Figure 5a). As indicated in Figure 5b, the position-dependent channel width also results in Dirac points shift of GNS found in the measured transfer characteristics. That is, the "narrow" tip part shows the Dirac point voltage (V_{Dirac}) of ≈25 V, while that of "wide" part shifts to a higher value of ≈38 V, suggesting heavier local *p*-doping in the wide part of GNS. Such width-dependent carrier density and its V_{GS} modulation are related by the following equation[25]

$$n = n_e - n_h = \frac{V_{GS} - V_{Dirac}}{e}\left(\frac{1}{C_{ox}} + \frac{1}{C_q}\right)^{-1} \quad (2)$$

where the quantum capacitance ($C_q \approx 10^{-6}$ F cm^{-2}) is much higher than the oxide capacitance ($C_{ox} \approx 10^{-8}$ F cm^{-2}) for a 300 nm SiO_2. Thus, Equation 2 can be further simplified for a carrier density (n) to

$$n = C_{ox}(V_{GS} - V_{Dirac})/e \quad (3)$$

The Fermi energy (E_F) can be calculated by $E_F = \hbar v_F k_F$,[25] and 2D Fermi wave vector k_F depends on the carrier density through $k_F = \sqrt{4\pi n/g_s g_v}$ with $g_s(g_v)$ being spin (valley) degeneracy factors of graphene ($g_s = g_v = 2$). Based on the above equations, i.e.,

$$E_F = \hbar v_F \sqrt{\pi n} \quad (4)$$

where v_F is the Fermi-Dirac velocity (1.1×10^6 ms^{-1}), the difference in the Fermi energy of the narrow and wide regions can be estimated to be ≈55 meV under the effective width approximation (see Fermi energy calculations in Supporting Information). The heavy doping of the graphene samples is responsible for the relatively low mobilities measured in this study.[26] So, the measured low mobility does not imply that the fabricated graphene samples is low.

As shown in Figure 5c, the width-dependent surface potential of GNS on copper substrate is further confirmed by Kelvin probe force microscopy (KPFM). Being measured along the white line (Inset in Figure 5c), it is clearly seen that the surface potential increases with width being increasing, suggesting more local *p*-type doping in the wider region of GNS. Such variation (≈60 meV) of surface potential along the scanned length of 5 μm within GNS is indeed comparable to that obtained from the shift of Fermi energy (55 meV) throughout the

© 2022 Wiley-VCH GmbH

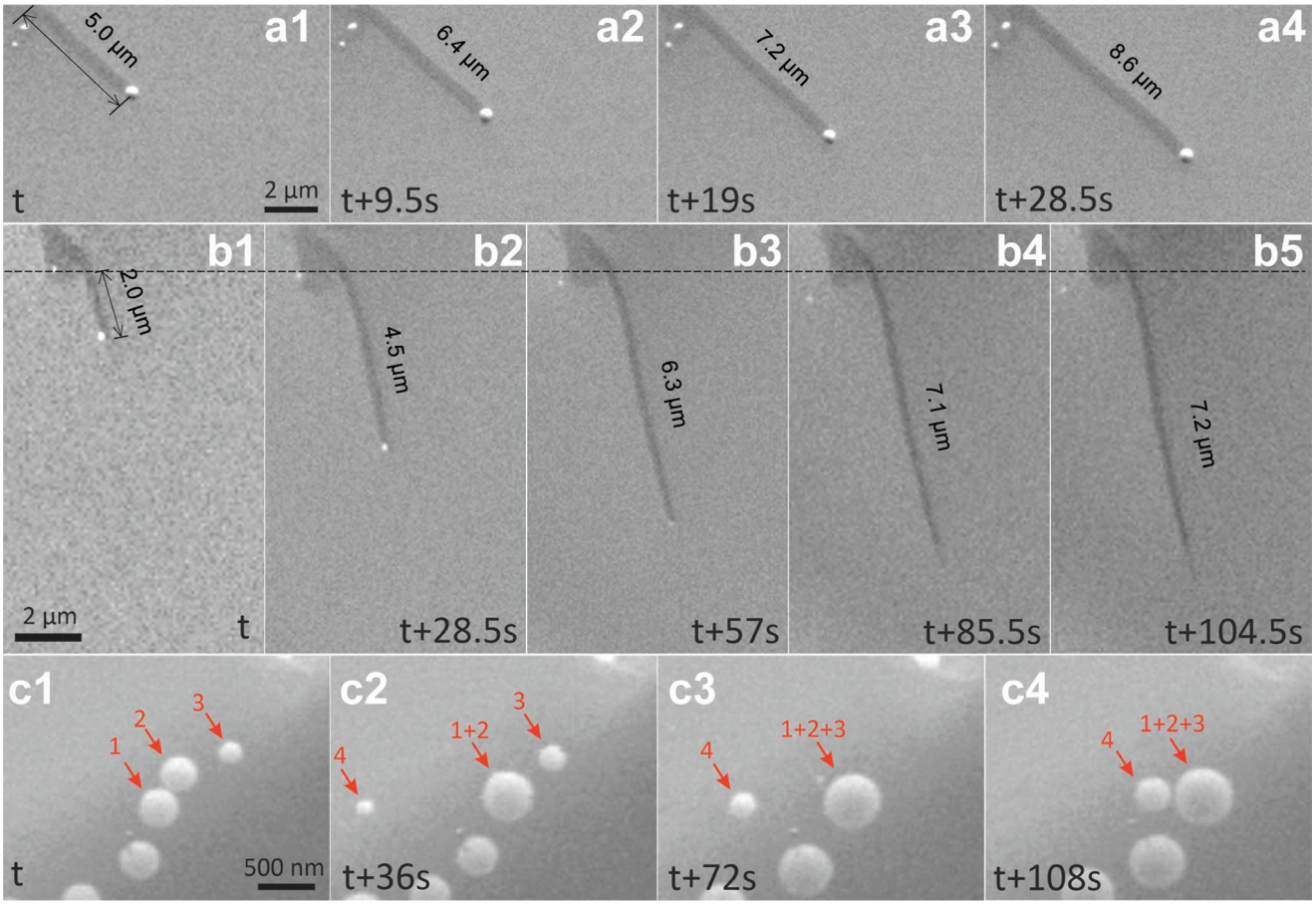

Figure 4. Time-laps image series recorded of VLS GNR growth on Cu foil. a1→a2→a3→a4,b1→b2→b3) The linear growth of two GNRs. b4→b5) GNR growth ceasing after run out of catalyst. c1→c2→c3→c4) Coalescence of liquid catalyst particles.

electrical transport measurements. Our combined characterizations demonstrate that GNS grown in a bottom-up manner is a promising candidate for electronic device applications with its tunable local Fermi energy in the channel.

3. Conclusion

The growth of GNSs that comprise a GNR by atmospheric pressure CVD has been reported, utilizing the propagation

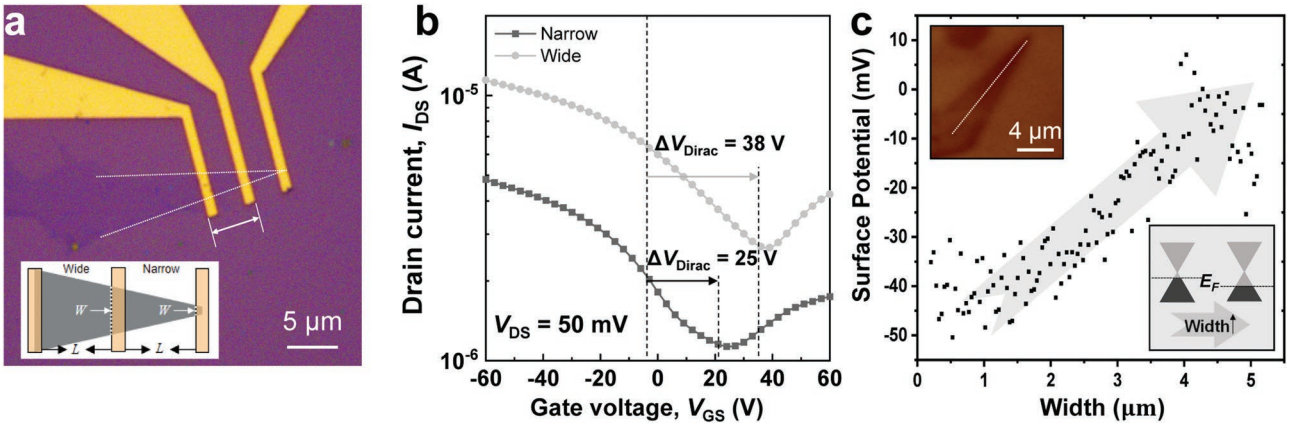

Figure 5. Electrical transport properties of GNS field-effect transistors (FETs) and their width dependent surface potential. a) Optical image of the back-gate FET devices with varying channel width. The channel length of the device was identically as 3 μm (5 μm when including two electrodes). b) Current–voltage transfer curves of the GNS FETs with different channel widths. They were fabricated on SiO_2/Si substrates and measured under V_{DS} = 50 mV. c) Surface potential of GNS determined by Kelvin prove force microscopy (KPFM) measurement. (Top) Inset is an image of the surface potential of GNS scanned along the white line. (Bottom) Inset shows a schematic drawing of width-dependent Fermi-level modification.

© 2022 Wiley-VCH GmbH

of liquid catalyst particles on a Cu surface. Controlling the H_2 flow during growth allows for the rates of VSS graphene growth and VLS GNR growth to be tuned. In turn, this controls the tip angle hence length and width of the GNS and potentially of the GNR. Controlling the dimensions along the GNS tip allows for selectivity regarding electronic properties, as the band gap of the material will depend on the width. Complete suppression of VSS graphene growth was directly observed by in situ SEM to preferentially grow a free standing GNR on Cu foil in an unparalleled way under relevant CVD conditions. It enables us to track the evolution behavior of VLS GNR growth during the real CVD process in real-time real-space with nanometer-scale resolution. These synthesized GNRs and GNSs show high carrier mobilities, and the doping levels of GNSs are found dependent on the width, which make them an excellent material for the Fermi-level tunable device applications. Achieving this level of control in CVD creates the first facile method under atmospheric conditions for synthesizing free-standing GNRs.

4. Experimental Section

Atmospheric Pressure CVD Growth of Graphene Nanospears on Cu Foils: Under atmospheric pressure (760 Torr), a polycrystalline Cu foil (Alpha Aesar#46365, 25 µm, 99.8 wt.%) was heated to 1050 °C in purified Ar gas (500 standard cubic centimeters per minute (sccm)) and then annealed for 60 min at this temperature in a mixed gas (500 sccm Ar, 200 sccm H_2). Next, after diluting (1%) in Ar, CH_4 (150 sccm) was added the constant mixed gas for 60 min. Finally, the sample was rapidly cooled to room temperature. The temperature-time profile is shown in Figure S1a (Supporting Information).

By tuning the experimental condition, GNSs with very sharp tips were achieved. As shown in Figure S1b (Supporting Information), the Cu foil was heated to 1000 °C in mixed gas (500 sccm Ar, 100 sccm H_2) and then annealed for 60 min. After that, purified CH_4 (5 sccm) and H_2 (300 sccm) was introduced the CVD chamber for 10 min. Finally, the sample was quickly cooled to room temperature.

In Situ Observations by Environmental SEM: In situ growth of GNR was performed inside the chamber of a modified environmental SEM system (Thermo Fisher Quattro S) with a custom infrared laser heating stage and with gas supplied station. The growth temperature arranged from 900 to 1000 °C under 40 Pa. Images were recorded by a large-field detector. During the experiments, the microscope was operated at an acceleration voltage of 3 kV. No influence of the electron beam on the growth and etching process could be observed. The imaged regions and their respective surroundings showed similar behavior, as evidenced by changing the magnification or by moving the sample under the beam. Furthermore, no electron beam induced contamination was observed at elevated temperatures.

Device Fabrication and Measurement: Prior to device fabrication, substrates (300 nm thick SiO_2/p^+-Si) were thoroughly cleaned up in piranha solution and by O_2 plasma treatment to remove any surface contamination. The grown nano-spear graphene flakes were then transferred to the substrates using PMMA (polymethyl methacrylate). The e-beam lithography equipment (NBL NB3) was used to produce source and drain patterns (beam current: 4.4 nA, Dose: 9.3 C m^{-2}), followed by e-beam evaporation of 10 nm Cr and 50 nm Au (Temescal FC-2000). A highly doped *p*-type Si was employed as a gate electrode. The semiconductor analyzer (Keithley 4200-SCS) was used to study the electrical transport properties of GNS field-effect transistors in a low-vacuum ($\approx 10^{-2}$ torr) probe station. The *I–V* characteristics between drain (0.05 V) and source (0 V) were measured at room temperature depend on back gating applied to the highly doped *p*-type Si substrate (−60 to 60 V).

Characterization: Optical images were obtained using an Olympus BX51 optical microscope. SEM images were conducted with an FEI Verios 460 environmental SEM field emission gun at 20 keV. AFM and KPFM data were performed with a Bruker Dimension Icon system. Raman spectra and maps were performed with a WITec scope with a 532 nm wavelength excitation Ar laser.

Supporting Information

Supporting Information is available from the Wiley Online Library or from the author.

Acknowledgements

H.S., F.L., L.Z., and K.K. contributed equally to this work. The authors acknowledge support from the Institute for Basic Science (IBS-R019-D1) of Republic of Korea. J.S. and K.K. are supported by the National Research Foundation of Korea (NRF) grants funded by the Korea government (MIST) (2020R1C1C1011219 and 2022M3H4A1A01013228).

Conflict of Interest

The authors declare no conflict of interest.

Data Availability Statement

The data that supports the findings of this study are available in the supplementary material of this article.

Keywords

chemical vapor deposition, graphene nanoribbons, graphene nanospears, growth mechanism

Received: July 2, 2022
Published online:

[1] a) T. Fang, A. Konar, H. Xing, D. Jena, *Phys. Rev. B* **2008**, *78*, 205403; b) Y. S. Shin, J. Y. Son, M. H. Jo, Y. H. Shin, H. M. Jang, *J. Am. Chem. Soc.* **2011**, *133*, 5623.

[2] a) R. Faccio, P. A. Denis, H. Pardo, C. Goyenola, Á. W. Mombrú, *J. Phys.: Condens. Matter* **2009**, *21*, 285304; b) D. Xia, Q. Li, Q. Xue, C. Liang, M. Dong, *Phys. Chem. Chem. Phys.* **2016**, *18*, 18406.

[3] a) M. H. Bae, Z. Li, Z. Aksamija, P. N. Martin, F. Xiong, Z.-Y. Ong, I. Knezevic, E. Pop, *Nat. Commun.* **2013**, *4*, 1734; b) J. Campos-Delgado, Y. A. Kim, T. Hayashi, A. Morelos Gomez, M. Hofmann, H. Muramatsu, M. Endo, H. Terrones, R. D. Shull, M. S. Dresselhaus, M. Terrones, *Chem. Phys. Lett.* **2009**, *469*, 177.

[4] a) V. Barone, O. Hod, G. E. Scuseria, *Nano Lett.* **2006**, *6*, 2748; b) Y. W. Son, M. L. Cohen, S. G. Louie, *Nature* **2006**, *444*, 347; c) Y. W. Son, M. L. Cohen, S. G. Louie, *Phys. Rev. Lett.* **2006**, *97*, 216803; d) M. Y. Han, B. Özyilmaz, Y. Zhang, P. Kim, *Phys. Rev. Lett.* **2007**, *98*, 206805; e) L. Yang, C. H. Park, Y. W. Son, M. L. Cohen, S. G. Louie, *Phys. Rev. Lett.* **2007**, *99*, 186801; f) R. M. Jacobberger, B. Kiraly, M. Fortin-Deschenes, P. L. Levesque, K. M. McElhinny, G. J. Brady, R. Rojas Delgado, S. Singha Roy, A. Mannix,

 © 2022 Wiley-VCH GmbH

M. G. Lagally, P. G. Evans, P. Desjardins, R. Martel, M. C. Hersam, N. P. Guisinger, M. S. Arnold, *Nat. Commun.* **2015**, *6*, 8006; g) A. R. Carvalho, J. H. Warnes, C. H. Lewenkopf, *Phys. Rev. B* **2014**, *89*, 245444.

[5] a) H. Wang, H. S. Wang, C. Ma, L. Chen, C. Jiang, C. Chen, X. Xie, A. P. Li, X. Wang, *Nat. Rev. Phys.* **2021**, *3*, 791; b) Z. Geng, B. Hähnlein, R. Granzner, M. Auge, A. A. Lebedev, V. Y. Davydov, M. Kittler, J. Pezoldt, F. Schwierz, *Ann. Phys.* **2017**, *529*, 1700033; c) J. P. Llinas, A. Fairbrother, G. Borin Barin, W. Shi, K. Lee, S. Wu, B. Yong Choi, R. Braganza, J. Lear, N. Kau, W. Choi, C. Chen, Z. Pedramrazi, T. Dumslaff, A. Narita, X. Feng, K. Müllen, F. Fischer, A. Zettl, P. Ruffieux, E. Yablonovitch, M. Crommie, R. Fasel, J. Bokor, *Nat. Commun.* **2017**, *8*, 633; d) X. Wang, Y. Ouyang, X. Li, H. Wang, J. Guo, H. Dai, *Phys. Rev. Lett.* **2008**, *100*, 206803.

[6] a) L. Jiao, X. Wang, G. Diankov, H. Wang, H. Dai, *Nat. Nanotechnol.* **2010**, *5*, 321; b) D. V. Kosynkin, A. L. Higginbotham, A. Sinitskii, J. R. Lomeda, A. Dimiev, B. K. Price, J. M. Tour, *Nature* **2009**, *458*, 872; c) L. Jiao, L. Zhang, X. Wang, G. Diankov, H. Dai, *Nature* **2009**, *458*, 877; d) C. Chen, Y. Lin, W. Zhou, M. Gong, Z. He, F. Shi, X. Li, J. Z. Wu, K. T. Lam, J. N. Wang, F. Yang, Q. Zeng, J. Guo, W. Gao, J. M. Zuo, J. Liu, G. Hong, A. L. Antaris, M. C. Lin, W. L. Mao, H. Dai, *Nat. Electron.* **2021**, *4*, 653.

[7] a) L. Ma, J. Wang, J. Yip, F. Ding, *J. Phys. Chem. Lett.* **2014**, *5*, 1192; b) X. Li, X. Wang, L. Zhang, S. Lee, H. Dai, *Science* **2008**, *319*, 1229; c) X. Wang, H. Dai, *Nat. Chem.* **2010**, *2*, 661; d) H. Sun, J. Dong, F. Liu, F. Ding, *Mater. Today* **2021**, *42*, 192.

[8] J. Cai, P. Ruffieux, R. Jaafar, M. Bieri, T. Braun, S. Blankenburg, M. Muoth, A. P. Seitsonen, M. Saleh, X. Feng, K. Müllen, R. Fasel, *Nature* **2010**, *466*, 470.

[9] X. Zhou, G. Yu, *Adv. Mater.* **2020**, *32*, 1905957.

[10] a) I. Ivanov, Y. Hu, S. Osella, U. Beser, H. I. Wang, D. Beljonne, A. Narita, K. Müllen, D. Turchinovich, M. Bonn, *J. Am. Chem. Soc.* **2017**, *139*, 7982; b) A. Narita, X. Feng, Y. Hernandez, S. A. Jensen, M. Bonn, H. Yang, I. A. Verzhbitskiy, C. Casiraghi, M. R. Hansen, A. H. R. Koch, G. Fytas, O. Ivasenko, B. Li, K. S. Mali, T. Balandina, S. Mahesh, S. De Feyter, K. Müllen, *Nat. Chem.* **2014**, *6*, 126.

[11] a) Z. Chen, W. Zhang, C. A. Palma, A. Lodi Rizzini, B. Liu, A. Abbas, N. Richter, L. Martini, X. Y. Wang, N. Cavani, H. Lu, N. Mishra, C. Coletti, R. Berger, F. Klappenberger, M. Kläui, A. Candini, M. Affronte, C. Zhou, V. De Renzi, U. del Pennino, J. V. Barth, H. J. Räder, A. Narita, X. Feng, K. Müllen, *J. Am. Chem. Soc.* **2016**, *138*, 15488; b) A. Candini, L. Martini, Z. Chen, N. Mishra, D. Convertino, C. Coletti, A. Narita, X. Feng, K. Müllen, M. Affronte, *J. Phys. Chem. C* **2017**, *121*, 10620; c) Z. Chen, H. I. Wang, J. Teyssandier, K. S. Mali, T. Dumslaff, I. Ivanov, W. Zhang, P. Ruffieux, R. Fasel, H. J. Räder, D. Turchinovich, S. De Feyter, X. Feng, M. Kläui, A. Narita, M. Bonn, K. Müllen, *J. Am. Chem. Soc.* **2017**, *139*, 3635.

[12] a) K. A. Simonov, N. A. Vinogradov, A. S. Vinogradov, A. V. Generalov, E. M. Zagrebina, N. Mårtensson, A. A. Cafolla, T. Carpy, J. P. Cunniffe, A. B. Preobrajenski, *J. Phys. Chem. C* **2014**, *118*, 12532; b) K. A. Simonov, N. A. Vinogradov, A. S. Vinogradov, A. V. Generalov, E. M. Zagrebina, G. I. Svirskiy, A. A. Cafolla, T. Carpy, J. P. Cunniffe, T. Taketsugu, A. Lyalin, N. Mårtensson, A. B. Preobrajenski, *ACS Nano* **2015**, *9*, 8997; c) C. Sánchez-Sánchez, T. Dienel, O. Deniz, P. Ruffieux, R. Berger, X. Feng, K. Müllen, R. Fasel, *ACS Nano* **2016**, *10*, 8006; d) F. Schulz, P. H. Jacobse, F. F. Canova, J. van der Lit, D. Z. Gao, A. van den Hoogenband, P. Han, R. J. M. Klein Gebbink, M. E. Moret, P. M. Joensuu, I. Swart, P. Liljeroth, *J. Phys. Chem. C* **2017**, *121*, 2896; e) J. D. Teeter, P. S. Costa, M. Mehdi Pour, D. P. Miller, E. Zurek, A. Enders, A. Sinitskii, *Chem. Commun.* **2017**, *53*, 8463.

[13] a) L. Chen, L. He, H. S. Wang, H. Wang, S. Tang, C. Cong, H. Xie, L. Li, H. Xia, T. Li, T. Wu, D. Zhang, L. Deng, T. Yu, X. Xie, M. Jiang, *Nat. Commun.* **2017**, *8*, 14703; b) H. S. Wang, L. Chen, K. Elibol, L. He, H. Wang, C. Chen, C. Jiang, C. Li, T. Wu, C. X. Cong, T. J. Pennycook, G. Argentero, D. Zhang, K. Watanabe, T. Taniguchi, W. Wei, Q. Yuan, J. C. Meyer, X. Xie, *Nat. Mater.* **2021**, *20*, 202.

[14] H. Suzuki, T. Kaneko, Y. Shibuta, M. Ohno, Y. Maekawa, T. Kato, *Nat. Commun.* **2016**, *7*, 11797.

[15] a) X. Li, W. Cai, J. An, S. Kim, J. Nah, D. Yang, R. Piner, A. Velamakanni, I. Jung, E. Tutuc, S. K. Banerjee, L. Colombo, R. S. Ruoff, *Science* **2009**, *324*, 1312; b) X. Xu, Z. Zhang, J. Dong, D. Yi, J. Niu, M. Wu, L. Lin, R. Yin, M. Li, J. Zhou, *Sci. Bull.* **2017**, *62*, 1074; c) R. Muñoz, C. Gómez-Aleixandre, *Chem. Vap. Deposition* **2013**, *19*, 297.

[16] a) J. Dong, L. Zhang, B. Wu, F. Ding, Y. Liu, *J. Phys. Chem. Lett.* **2021**, *12*, 7942; b) J. Dong, L. Zhang, F. Ding, *Adv. Mater.* **2019**, *31*, 1801583; c) L. Zhang, J. Dong, F. Ding, *Chem. Rev.* **2021**, *121*, 6321.

[17] R. S. Wagner, W. C. Ellis, *Appl. Phys. Lett.* **1964**, *4*, 89.

[18] V. L. Nguyen, D. L. Duong, S. H. Lee, J. Avila, G. Han, Y. M. Kim, M. C. Asensio, S. Y. Jeong, Y. H. Lee, *Nat. Nanotech.* **2020**, *15*, 861.

[19] a) K. Sufryd, N. Ponweiser, P. Riani, K. W. Richter, G. Cacciamani, *Intermetallics* **2011**, *19*, 1479; b) H. Okamoto, *J. Phase Equilib. Diffus.* **2012**, *33*, 415.

[20] a) I. Vlassiouk, M. Regmi, P. Fulvio, S. Dai, P. Datskos, G. Eres, S. Smirnov, *ACS Nano* **2011**, *5*, 6069; b) B. Wu, D. Geng, Z. Xu, Y. Guo, L. Huang, Y. Xue, J. Chen, G. Yu, Y. Liu, *NPG Asia Mater.* **2013**, *5*, e36; c) D. Geng, B. Wu, Y. Guo, L. Huang, Y. Xue, J. Chen, G. Yu, L. Jiang, W. Hu, Y. Liu, *Proc. Natl. Acad. Sci. USA* **2012**, *109*, 7992; d) T. Ma, W. Ren, X. Zhang, Z. Liu, Y. Gao, L.-C. Yin, X. L. Ma, F. Ding, H. M. Cheng, *Proc. Natl. Acad. Sci. USA* **2013**, *110*, 20386.

[21] Z. J. Wang, J. Dong, Y. Cui, G. Eres, O. Timpe, Q. Fu, F. Ding, R. Schloegl, M. G. Willinger, *Nat. Commun.* **2016**, *7*, 13256.

[22] a) M. Morales Alfredo, M. Lieber Charles, *Science* **1998**, *279*, 208; b) Y. Wu, P. Yang, *J. Am. Chem. Soc.* **2001**, *123*, 3165; c) P. J. F. Harris, *Carbon* **2007**, *45*, 229; d) J. Gavillet, J. Thibault, O. Stéphan, H. Amara, A. Loiseau, C. Bichara, J. P. Gaspard, F. Ducastelle, *J. Nanosci. Nanotechnol.* **2004**, *4*, 346; e) A. J. Page, F. Ding, S. Irle, K. Morokuma, *Rep. Prog. Phys.* **2015**, *78*, 036501.

[23] a) S. Li, Y. C. Lin, W. Zhao, J. Wu, Z. Wang, Z. Hu, Y. Shen, D.-M. Tang, J. Wang, Q. Zhang, H. Zhu, L. Chu, W. Zhao, C. Liu, Z. Sun, T. Taniguchi, M. Osada, W. Chen, Q. H. Xu, A. T. S. Wee, K. Suenaga, F. Ding, G. Eda, *Nat. Mater.* **2018**, *17*, 535; b) X. Li, B. Li, J. Lei, K. V. Bets, X. Sang, E. Okogbue, Y. Liu, R. R. Unocic, B. I. Yakobson, J. Hone, A. R. Harutyunyan, *Sci. Adv.* **2021**, *7*, eabk1892.

[24] F. Liu, J. Dong, N. Y. Kim, Z. Lee, F. Ding, *Small* **2021**, *17*, 2103484.

[25] R. Fates, H. Bouridah, J. P. Raskin, *Carbon* **2019**, *149*, 390.

[26] a) J. H. Gosling, O. Makarovsky, F. Wang, N. D. Cottam, M. T. Greenaway, A. Patanè, R. D. Wildman, C. J. Tuck, L. Turyanska, T. M. Fromhold, *Commun. Phys.* **2021**, *4*, 30; b) L. Banszerus, M. Schmitz, S. Engels, J. Dauber, M. Oellers, F. Haupt, K. Watanabe, T. Taniguchi, B. Beschoten, C. Stampfer, *Sci. Adv.* **2015**, *1*, e1500222.

© 2022 Wiley-VCH GmbH